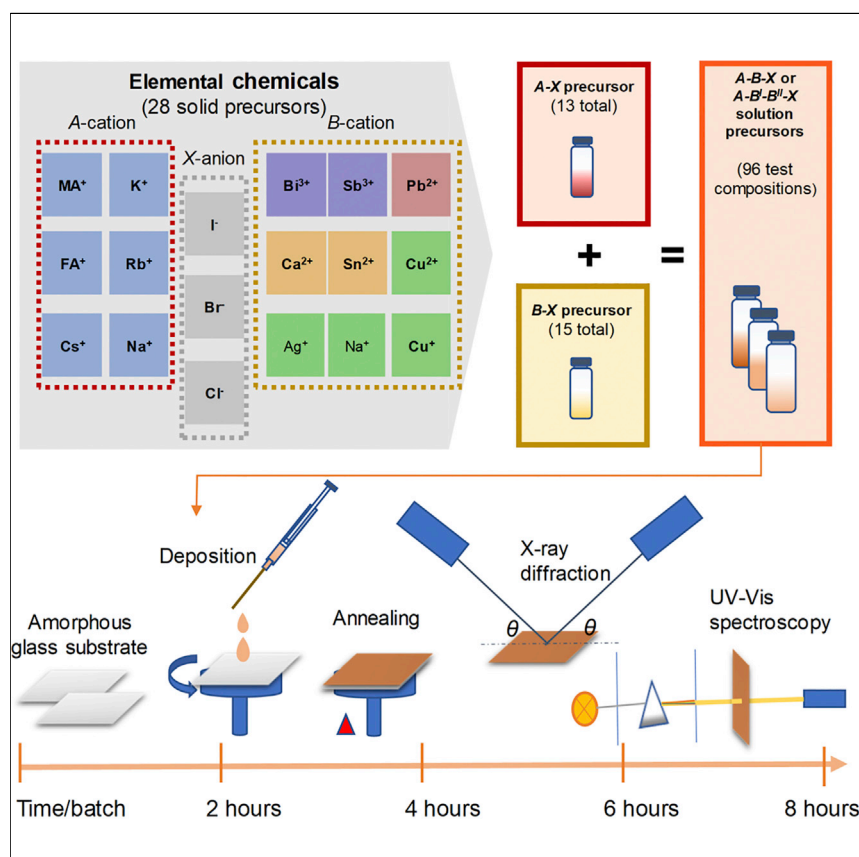**Article**

Accelerated Development of Perovskite-Inspired Materials via High-Throughput Synthesis and Machine-Learning Diagnosis

Fast experimental cycles enable exploration of wide chemical space and data-driven analysis.

Shijing Sun, Noor T.P. Hartono, Zekun D. Ren, ..., Ian Marius Peters, Juan-Pablo Correa-Baena, Tonio Buonassisi

shijings@mit.edu (S.S.)
buonassisi@mit.edu (T.B.)

HIGHLIGHTS

Investigation of 75 perovskite-inspired compositions in thin-film form (41 Pb free)

A deep neural network classifies perovskites into 0D, 2D, and 3D structures

Non-linear band-gap behavior discovered in $Cs_3(Bi_{1-x}Sb_x)_2(I_{1-x}Br_x)_9$ dual-site alloys

Joule

CellPress

Article

Accelerated Development of Perovskite-Inspired Materials via High-Throughput Synthesis and Machine-Learning Diagnosis

Shijing Sun,[1,*] Noor T.P. Hartono,[1] Zekun D. Ren,[1,2] Felipe Oviedo,[1] Antonio M. Buscemi,[1] Mariya Layurova,[1] De Xin Chen,[1] Tofunmi Ogunfunmi,[1] Janak Thapa,[1] Savitha Ramasamy,[3] Charles Settens,[4,5] Brian L. DeCost,[5] Aaron G. Kusne,[5] Zhe Liu,[1] Siyu I.P. Tian,[1,2] Ian Marius Peters,[1] Juan-Pablo Correa-Baena,[1] and Tonio Buonassisi[1,2,6,*]

SUMMARY

Accelerating the experimental cycle for new materials development is vital for addressing the grand energy challenges of the 21st century. We fabricate and characterize 75 unique perovskite-inspired compositions within a 2-month period, with 87% exhibiting band gaps between 1.2 and 2.4 eV, which are of interest for energy-harvesting applications. We utilize a fully connected deep neural network to classify compounds based on experimental X-ray diffraction data into 0D, 2D, and 3D structures, more than 10 times faster than human analysis and with 90% accuracy. We validate our methods using lead-halide perovskites and extend the application to lead-free compositions. The wider synthesis window and faster cycle of learning enables the realization of a multi-site lead-free alloy series, $Cs_3(Bi_{1-x}Sb_x)_2(I_{1-x}Br_x)_9$. We reveal the non-linear band-gap behavior and transition in dimensionality upon simultaneous alloying on the B-site and X-site of $Cs_3Bi_2I_9$ with Sb and Br.

INTRODUCTION

Despite sustained community interest in perovskite-inspired solar cells,[1] progress in realizing a suitable lead-free material has been slow.[2,3] The combination of high-throughput experiments and machine learning offers a new approach to exploring the rich physics of these materials in device-relevant thin-film form.[4] Herein, we access a wide range of lead-halide and lead-free perovskites within a singular liquid-synthesis thin-film growth environment by assembling a set of Pb-, Sn-, Bi-, Sb-, Ag-, Cu-, and Na-rich precursors and anti-solvent (chlorobenzene). In a 2-month period, we create 96 unique precursor solutions, which were synthesized using 28 solid precursors based on recently developed Pb, Sn, Bi, Sb, Cu, and Ag compounds.[5,6] 75 unique chemical compositions were deposited into crystalline thin films (based on X-ray diffraction [XRD]); among them, 65 exhibit band gaps between 1.2 and 2.4 eV (assuming direct band gaps), of strong interest for a range of energy-harvesting applications, e.g., single-junction and tandem photovoltaic (PV) devices.[7] This increased rate of synthesis motivates the development of high-throughput, automated characterization.[8] We acquire XRD data in 10 min or less using a high scan rate over a θ-2θ geometry and use a 3-layer (256-256-256) dense neural network to analyze the structural dimensionality of experimental data with 90% accuracy. The network is trained partially with augmented data from the Inorganic Crystallographic Structure Database (ICSD)[9] to overcome the sparse data

Context & Scale

To meet increasing global energy demand, it is critical yet challenging to accelerate the development of novel energy materials. High-throughput experimentation (HTE) and machine-learning techniques have become increasingly accessible to scientific researchers. We herein demonstrate a case study on perovskite-inspired materials, where a combination of fast synthesis and machine-learning-assisted data diagnostics of 75 compositions achieves an acceleration of over an order of magnitude per experimental learning cycle over our laboratory baseline. The increased throughput and streamlined workflow enable the realization of new candidate photovoltaic materials, which sheds light on the search for lead-free perovskites in this multi-parameter chemical space. Our study demonstrates that combining an accelerated experimental cycle of learning and machine-learning-based diagnosis represents an important step toward realizing fully automated laboratories for materials discovery and development.

Joule

problem due to the small experimental dataset. The combination of a wide range of precursors and solvent engineering significantly enlarges the chemical space explored, providing a platform to study the composition map with both single- and dual-site alloying. Compounds and their alloys targeted and synthesized in this study span ABX_3, $A_3B_2X_9$, ABX_4, and $A_2B^I B^{III} X_6$ (A = MA, FA, Cs, Rb, K, or Na; B = Pb, Sn, Ag, Cu, Na, Bi, or Sb; and X = Cl, Br, or I) perovskite-inspired materials with 0D, 2D, or 3D crystallographic structures.

Our dual focus on experimental throughput and learning rate is motivated by the growing gap between theory and experiment. The application of machine-learning techniques to assist the discovery and understanding of energy materials has attracted increasing attention in recent years; for example, Suram et al. reported an automatic phase mapping algorithm for metal oxide light absorbers.[10] Gaultois et al. developed web-based models for the screening of thermoelectric materials.[11] In the PV community, several studies investigated the use of machine-learning techniques in combination with density functional theory (DFT) calculations to search for new chemical space,[12,13] yet few reports have focused on accelerating the diagnostics in the experimental cycle.[14] Over one thousand perovskite-inspired candidate compounds have been theoretically predicted during the last few years;[15–17] a triumph of modern first-principles DFT simulations, high-performance computing hardware, and the resulting searchable databases of materials properties.[18,19] Many studies proposed to replace the toxic Pb^{2+} in methylammonium lead iodide (MAPI) and the unstable Sn^{2+} in $MASnI_3$ with Bi^{3+}/Sb^{3+}, forming zero- or two-dimensional $A_3B_2X_9$ compounds, or three-dimensional $A_2B^I B^{III} X_6$ double perovskites.[20,21] In contrast to the high throughput of theoretical predictions, only a small fraction of predicted compounds have been experimentally realized.[22] A few dozen Pb-free MAPI-inspired compounds were explored, often first by relatively lower-throughput bulk-crystal synthesis.[3,23] Among those, Sn perovskites have achieved over 9% efficiency,[24] while the air-stable iodide-based $A_3B_2I_9$ (A = Cs, Rb, MA, or NH_4; and B = Bi or Sb) and the bromide-based double perovskite $Cs_2AgBiBr_6$ have recently been incorporated into PV devices with champion efficiencies over 2%.[20,25,26]

Fast exploration of novel thin-film compositions encounters many practical obstacles, in part because of the complex thermodynamic phase formation of ternary and quaternary compounds, in addition to the unknown kinetics.[5,27] It is time consuming to access a wide range of the periodic table and possible process windows via bulk-crystal growth. Furthermore, transforming bulk crystals to the device-relevant thin-film form can be challenging since p-block cations typically have low solubilities in common solvents and process windows are typically less tunable. This often leads to a slow learning rate that favors incremental trial and error,[8] and that is at odds with the timelines of many investors and the residency time of individual researchers.[28] As a result, many key breakthroughs, including MAPI solar cells, were discovered rather than predicted.[29] The "experimental bottleneck" limits material development both directly and indirectly, e.g., by slowing experimental feedback to improve the predictive accuracy of theoretical models, reducing the success of the inverse-design paradigm (Figure S1).

By increasing experimental throughput without sacrificing material quality, we report the synthesis and characterization of 75 halide perovskite compositions, including 17 compounds and 58 alloy compositions. To our best knowledge, four compounds are reported in thin-film form for the first time, all of which are lead free. Among the alloys, 18 lead-free perovskite alloys are studied, which doubles the number of known inorganic thin-film compositions with lead-free perovskite-related architectures.[19]

[1]Photovoltaic Research Laboratory, Massachusetts Institute of Technology, Cambridge, MA 02139, USA

[2]Singapore-MIT Alliance for Research and Technology, Singapore 138602, Singapore

[3]Institute of Infocomm Research, A*STAR, Singapore 138632, Singapore

[4]Materials Research Laboratory, Massachusetts Institute of Technology, Cambridge, MA 02139, USA

[5]Materials Measurement Science Division, National Institute of Standards and Technology, Gaithersburg, MD 20899, USA

[6]Lead Contact

*Correspondence: shijings@mit.edu (S.S.), buonassisi@mit.edu (T.B.)

https://doi.org/10.1016/j.joule.2019.05.014

Joule

Among them, we present the first Pb-free dual-site alloy series, $Cs_3(Bi_{1-x}Sb_x)_2$ $(I_{1-x}Br_x)_9$, which exhibits a transition between 0D to 2D crystal structures and non-linear band-gap tunability. The discovery of non-linear band-gap behavior in this series opens a new pathway to achieve lead-free all-inorganic perovskites for multi-junction solar cells.

In the next sections, we describe how we narrow the "throughput gap" between experiment and theory in three steps: first, we perform each step by hand, quantify our workflow using a timer, and then optimize our workflow to reduce inefficiencies;[30,31] second, we develop a synthesis platform capable of accessing a wide range of precursors to evaluate multiple classes of material within an equivalent time; and third, we adapt and harness statistical and machine-learning tools to accelerate data acquisition and analysis.[30,31] We believe that these three steps are broadly applicable to other functional and structural materials searches, given similarly reported mismatches between the time needed for each theory and the experimental cycle of learning. Notably, these improvements result in a 35× throughput improvement over our laboratory baseline even before implementing systematic and automated solutions; further gains of 10–100× can be expected by fully automating our workflow.

RESULTS AND DISCUSSION

Workflow Optimization and Precursor Development for a Robust, Flexible Synthesis Platform

We undertook a multi-year workflow-optimization effort in our laboratory, designed to quantify and reduce the time taken for each step in thin-film synthesis and diagnosis (Figure S2). The goal of our workflow-optimization effort is to maximize "usable information per unit time." We set a target of 35 high-quality compositions synthesized and analyzed per month (both phase and band-gap diagnosis, Figure 1) and targeted a batch throughput of 150 samples per month in our synthesis loop. This throughput is 35× faster than our previous laboratory baselines of PV device fabrication based on other deposition methods,[32–34] approaching the throughputs of high-throughput experimentation (HTE) platforms developed for other materials classes.[4,30,31,35] This allowed an experimental capacity of one cycle of learning per batch per day, including optical and structural characterization, with several candidate materials per batch. Traditionally, the term "HTE" refers specifically to the application of combinatorial deposition, automation, or both. In this study, we achieve an order-of-magnitude acceleration via "workflow ergonomics" and judicious application of machine learning to accelerate low-throughput characterization tools. We use the term "high throughput" to reflect the order-of-magnitude acceleration, with these qualifications.

Such a fast accumulation of experimental data motivates the development of automated data analysis. Our workflow analysis identified "structural characterization" as an experimental bottleneck limiting the learning rate per sample (Figures S3 and S4). In this study, we adapt and apply a neural network to assist with phase identification,[36,37] which enables us to classify and test the crystallographic dimensionality of perovskite-inspired materials within 2 min, including the time for training and within a second after the training in this study. In the context of halide perovskites, the dimensionality of a compound refers to the connectivity of the inorganic framework, e.g., a 3D perovskite, $MAPbI_3$, consists of corner-sharing PbI_6 octahedra extended into a 3D network. It has been shown that the electronic mobility of a halide perovskite material is closely related to its crystallographic dimensionality and a high dimensionality is preferred.[17] Among the Pb-free solar cells, 2D
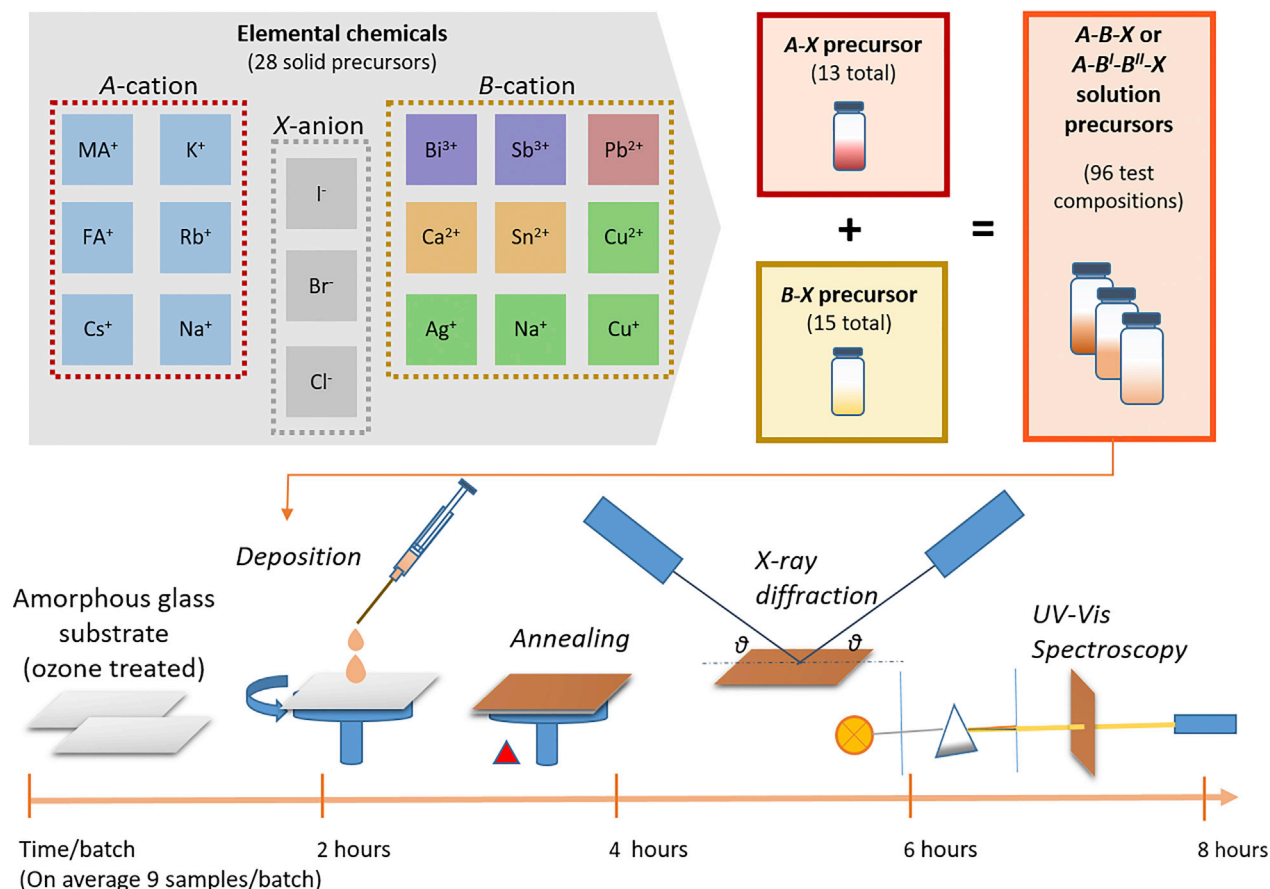
Figure 1. Sketch of the Optimized Experimental Workflow Employed in This Study

A typical perovskite is a ternary compound with ABX_3 architecture. Precursor solutions of 96 perovskite-inspired target compositions were prepared by mixing the commercially available A-X and B-X solid precursors in stoichiometric ratios. Six cations from the periodic table were dissolved as A-site cations in the target compounds, together with nine cations for the B-site and three halide ions for the X-site. 28 solid precursors, which include 13 A-X (e.g., CsI) and 15 B-X (e.g., BiI_3), were used in this study). Through one cycle of learning, each successfully prepared precursor solution follow the three experimental steps of thin-film deposition, X-ray diffraction, and UV-visible (UV-vis) spectroscopy measurement to examine the structure and optical properties. Candidate thin films are screened based on their band gap and the formation of crystalline phases.

perovskites show superior performance than their 0D perovskite counterparts.[38] "Dimensionality" is chosen as a crystal descriptor (i.e., output parameter of merit) in this study because of recent reports linking charge-transport behavior to higher dimensionality, whereas low-dimensional perovskites tend to exhibit higher stability.[2,39–44] In this study, the dimensionality labels are determined based on the space group and elemental information in the ICSD. Because the amount of labeled data from experimentation alone is too small to adequately train a neural network, we augment experimental training data with powder X-ray diffraction (PXRD) patterns computed from the ICSD. As discussed in the next section, in addition to classification, the neural network can also diagnose the dimensionality of novel materials. For compositions previously reported in the literature, both band-gap and XRD patterns were cross-checked with literature data.[45–48]

To test a wide composition space while avoiding false negatives, a robust yet flexible synthesis platform is essential. Solution synthesis (e.g., spin coating) of perovskite-inspired thin-film materials is fast but requires liquid precursors amenable to spin coating.[49] A typical perovskite composition used in recent solar cells consists of
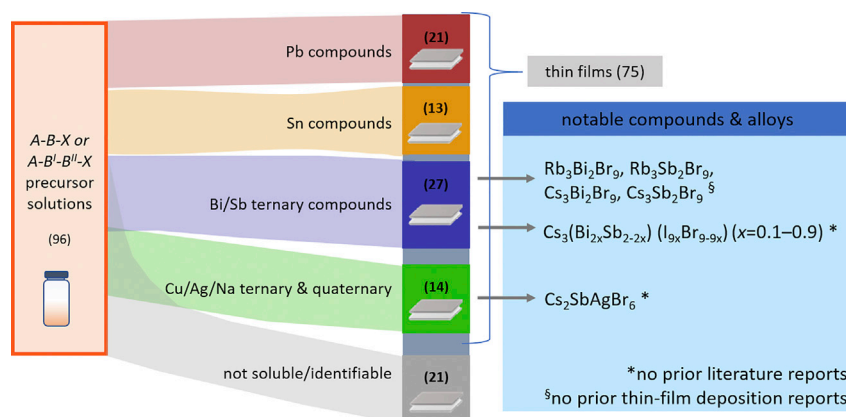
Joule

Figure 2. Sankey Diagram Demonstrating the Material Synthesis Flow of the 96 Precursor Compositions Attempted, of which 75 Resulted in Thin Films

an ABX_3 architecture where A is a monovalent cation, B is lead, and X is a halide. Historically, the range of precursors was limited, given the low solubilities of p-block cations and alkaline earth metals in common solvents. Recently, our laboratory developed Sb and Bi precursors.[50,51] We use these precursors, as well as the commonplace Pb and Sn,[45,52] and the Ag and Cu precursors recently reported in the literature,[3,53] to centralize our stock solution for synthesis and streamline the parameter space of processing conditions with solvent engineering (Tables S1 and S2). We hereto select a list of 96 perovskite-inspired target compositions for this study by a combination of literature,[6,51,53–57] theory,[16,18] and in-house research (Tables S3 and S4). Using these test compositions, we attempt to synthesize the recently computationally predicted or experimentally realized material classes in thin-film form.[15,18] The synthesis includes the following five perovskite-related crystal systems: ABX_3 (3D), $A_3B_2X_9$ (2D), $A_3B_2X_9$ (0D), ABX_4 (2D), and the 3D double perovskite $A_2B^IB^{II}X_6$ (A = MA, FA, Cs, Rb, K, or Na; B = Pb, Sn, Ag, Cu, Na, Bi, or Sb; and X = Cl, Br, or I). Precursor solutions were prepared with the stoichiometric ratios of the elements according to the target compositions respectively (Table S3). Universal solubility test and thin-film deposition methods were applied to access the solution processability of each material in the common organic solvents N,N-dimethylformamide (DMF) and dimethyl sulfoxide (DMSO). To ensure reproducibility, we synthesized an average of three films per composition. Repetitive synthesis of the key material series is listed in Table S9, where the results are used to train the machine-learning algorithm.

We focus our study on four classes of B-site cation (Figure 2): Pb-based ABX_3 single perovskites, Sn-based ABX_3 perovskite alloys, Bi- and Sb-rich $A_3B_2X_9$ low-dimensional perovskite-inspired materials, and Cu-, Ag-, and Na- rich perovskite-inspired materials. These four classes represent the well-established compositions (Pb- and Sn-rich), compositions explored mostly in the bulk forms (Bi and Sb rich), and lesser explored compositions (Cu, Ag, and Na rich), respectively. As shown in Figure 2, 75 out of the 96 attempted test compositions successfully yielded crystalline thin films. Among these 75 compositions, 21 are Pb-halide perovskite dual-site alloys based on $FAPbI_3$, $MAPbBr_3$, and $FAPbBr_3$; $MA_{1-x}FA_xPbI_xBr_{3-x}$; and $(Cs_{0.05}Rb_{0.05}MA_{0.9-x}FA_x)PbI_xBr_{3-x}$. We deposited the Pb-based thin films following literature deposition methods as a reference for our workflow timeline and verification for the machine-learning techniques.[45,54] 13 compositions are Sn-rich perovskites alloys based on $MASnI_3$, $MASn_{1-x}Ca_xI_3$, and $MASn_{1-x}Pb_xI_{3-x}Br_x$. In the search of lead-free
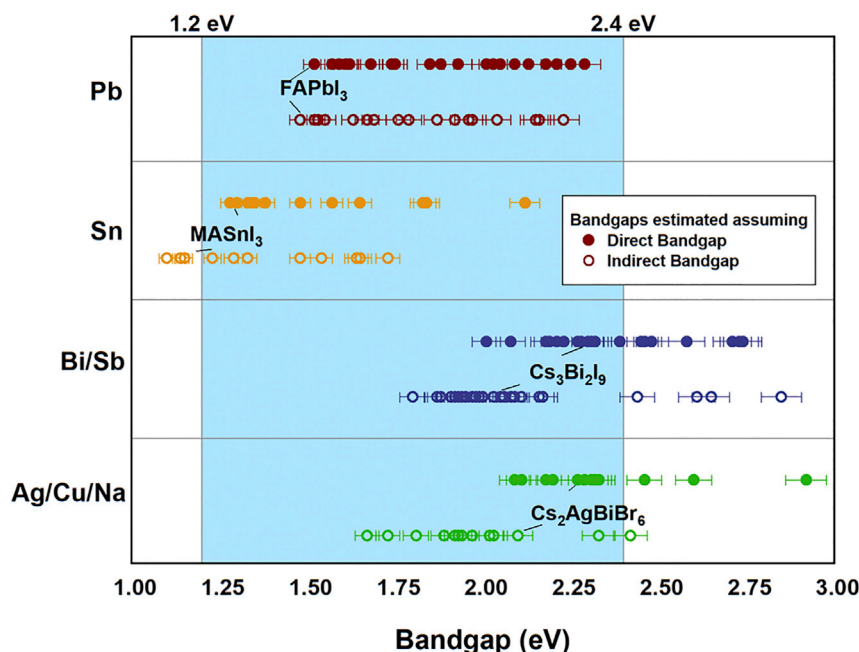
Figure 3. Band Gaps Measured for the 75 Thin-Film Compositions Investigated in This Study
Band gaps of each material were extracted from Tauc plots (2% errors), 65 of the 75 compositions show band gaps between 1.2 and 2.4 eV, assuming direct band gaps. Solid dots, band gaps estimated assuming direct band gap; circles, band gaps estimated assuming indirect band gap.

compositions, we deposited 28 Bi- and Sb-based compositions, including 10 compounds and 18 alloys. The successfully characterized structures include $A_3B_2X_9$ (A = Cs or Rb; B = Bi or Sb; and X = I or Br), $Cs_3(Bi_xSb_{1-x})I_9$, and $Cs_3(Bi_{1-x}Sb_x)_2(I_{1-x}Br_x)_9$. Finally, we explore 13 compositions (3 compounds and 10 alloys) that incorporate Ag, Cu, and Na in the precursor with perovskite-like stoichiometry of MA_2CuX_4 (X = Cl or Br) and $A_2B^IB^{II}X_6$ double perovskites (A = Cs or Rb; B^I = Bi or Sb; B^{II} = Ag, Cu, or Na; and X = I or Br) (Figures S5–S7).[57] In addition to the 75 compositions made into thin films, we discard 21 precursor solutions at the thin-film deposition stage, most of which belong to the Cu, Ag, or Na ternary and quaternary compound class (Table S8). The unsuccessful syntheses are attributed to the low solubility of the reactants in the solution (e.g., cesium acetate with silver bromide) or no products formed within processing window (e.g., Na_3B_2X9 [B = Sb and Bi]).

Figure 3 presents the optical properties of the 75 thin films grouped by B-site compositions. We measured the reflection and transmission of each film, and band gaps were deduced from Tauc plots (Figures S8–S10).[58] Both direct and indirect band gaps were calculated from measurements of freshly made films within a day, to avoid prior bias on the unknown crystal structures and any degradation. The linear region in the Tauc plots near the band edge was used to estimate the band gaps, and depending on the nature of the materials, samples exhibit direct or indirect band-gap characteristics. While Figure 3 presents results from both direct and indirect band gap assumptions for each material, the variation in band gaps between the two methods should be neglected (see Supplemental Information). It is well established that introduction of Br on the X-site of MAPbI$_3$ increases the band gap from 1.5 (0% Br) to 2.35 eV (100% Br).[59] The results from our measurements confirm this trend with mixed cation and halide alloys. In the case where both Br and Sn are alloyed into MAPbI$_3$ simultaneously, our results indicate that adding PbBr$_2$ into the MASnI$_3$

Joule

CellPress

system increases the band gap. This suggests that the effect of Br substitution for I has a more dominant effect than Pb substitution for Sn, an effect one might assume to be influenced by relative differences in electronegativity between substituting atomic pairs.[52] Furthermore, we tested 62 (out of 96) Pb-free and Sn-free target compounds and alloys in this study and 41 of them yielded compact films with no visible holes. We expand the known inorganic Bi and Sb halide perovskite deposition methods from iodide to bromide, the latter has received much less attention, and successfully developed $A_3B_2Br_9$ (A = Cs or Rb and B = Bi or Sb) thin films. This further enables us to explore a range of multi-site alloys within the Bi and Sb material classes and achieved a band gap tuning between 1.2 and 2.4 eV via compositional engineering.

Machine-Learning-Assisted Structural Diagnostics

A neural network is applied in this study to extract the materials descriptor, "dimensionality," from hundreds of experimental PXRD patterns. Upon manual phase identification,[47,60,61] 55 out of the 75 compositions are first identified with seven space groups (Table S7), belonging to three crystallographic dimensionalities where 11 are 0D (molecular dimers, e.g., $Cs_3Bi_2I_9$), 10 are 2D (layered perovskites, e.g., $Cs_3Sb_2Br_9$), and 34 are 3D (conventional perovskites, e.g., $MASnI_3$ and $CsAgBiBr_6$) (Figure S12). While it is promising to replace future human synthesis with robotics,[22] we soon realize that the traditional methods of analyzing XRD data are far slower than the rate of high-throughput film deposition and require significant human expertise along with prior knowledge of the expected crystal structures. Our accelerated material development paradigm tackles this issue by implementing a fully connected deep neural network classifier based on X-ray diffraction peak positions, allowing a rapid experimental screening of candidate materials based on structural features. We made a detailed comparison of various classification techniques and data augmentation algorithms in our parallel study on machine-learning method development to tackle the sparse data problem in XRD diagnostics using 115 thin-film samples, where the technical advantages in speed and accuracy of the deep neural network in this study were discussed.[62]

In order to learn effective XRD representations in the context of our small (<100 samples) dataset, we applied a transfer learning approach. A training dataset was first built consisting of 164 PXRD patterns, and their structural labels were extracted from ICSD (Table S7). Single, double, ternary, and quaternary combinations of the elements and space groups of interest were covered in this data mining, featuring the target 0D, 2D, and 3D perovskite materials and potential byproducts (precursors). To better account for the difference between the simulated powder patterns from the crystallography database and the experimental thin-film diffraction patterns, both simulated patterns and experimental patterns were subjected to a data augmentation process of sequential random peak scaling and elimination and peak position shifting to account, respectively, for the preferred orientation and substrate-induced strain in the thin-film samples. After the data augmentation process (see Supplemental Information for data argumentation processes), 2,000 XRD experimental patterns and 2,000 simulated patterns with corresponding dimensionality labels are obtained.

We use the whole dataset to train a fully connected, deep feedforward neural network, consisting of three hidden layers with *rectifying linear unit* activation functions of 256 neurons each.[63,64] The input layer consists of a vector of 1,350 elements, corresponding to the measured or simulated XRD intensities with a 2-theta step of 0.04°. The output layer is composed of 3 elements, corresponding to the 3 dimensionalities. The output layer uses a *softmax* activation function so that the neural

Joule

network outputs can be approximately interpreted as probabilities for each potential dimensionality. The weight optimization to minimize a log-loss function was performed by stochastic gradient descent (constant learning rate of 0.01).[65] $L2$ regularization with a λ of 0.0001 was used, and the maximum number of training epochs is set to 400, with an optimization tolerance rate of 1e−09 (Figure S14).[62] The accuracy of the test model is defined as the number of correctly labeled XRD patterns among the whole testing dataset, independent of class, compared to the ground-truth labels in ICSD. To verify the network is learning correctly, the first approach makes use of only the simulated training set for testing; in this approach, a mean model accuracy of 99% is achieved using 5-fold cross-validation (Table S5).

The second approach consists of using the simulated XRD patterns as a training dataset and the experimental patterns as a testing dataset using the same neural network architecture and hyperparameters. A mean model accuracy of 76% is obtained for 5-fold cross-validation. Although the data augmentation provides an improvement compared to a baseline classification accuracy of less than 60% when non-augmented data are used for training, using only simulated XRD patterns for training seems to capture all the subtle differences among experimental XRD patterns, such as systematic experimental error in sample alignment and random human errors in synthesis. To accurately capture these experimental features, the collected PXRD patterns for the 75 unique compositions are subdivided into two experimental datasets: *group 1*—manually identified perovskites with space group and dimensionality labels (55) and *group 2*—materials without structure details reported.[19] Figure 4A represents the schematic illustration of the third approach, where the final training dataset consists of simulated and randomly selected 80% of the *group 1* experimental pattern. Subsequently, after cross-validation, the blindfold model accuracy of 90% is achieved for *group 1* materials. Significant improvement in the model accuracy and robustness is demonstrated using the experimental data as part of the training set (Figure S13). Examples of experimental XRD patterns are shown in Figure 4B.

Figure 4C depicts the classification of the 75 unique compositions into three crystallographic dimensionalities based on the third machine-learning approach, where a confidence score between 0 and 1 is assigned to 0D, 2D, and 3D based on the *softmax* activation function outputs from the neural network, respectively for each composition. The *softmax* activation function assigns decimal probabilities to each class in a multi-class problem, and a confidence score of >0.5 indicates the suggested dimensionality of a given material (Table S6).[64] Most data points in Figure 4C cluster at the vertex of the triangle; the neural network classifier successfully separated the materials with different crystallographic dimensionalities with a relatively high confidence score. Considering the four materials classes synthesized in this study, Pb (yellow data points in Figure 4C) and Sn (cyan) perovskites in this study exhibit high confidence scores that point to 3D structures, which are consistent with the structural labels from a large number of literatures on ABX_3 (A = MA or FA, B = Pb or Sn, and X = I or Br).[18,45] The addition of Ag, Cu, or Na in the halide-perovskite-inspired materials (navy), results in various mixed phases that are challenging to identify. For example, the composition Ag + Cs + Bi + Br shows a confidence score of 0.98 for the 3D dimensionality (which comprises space groups Pm$\bar{3}$m, I4/mcm, or Fm$\bar{3}$m); the compound was in fact confirmed to exhibit the same PXRD pattern as the reported 3D double perovskite, $Cs_2AgBiBr_6$.[3] On the other hand, it is likely that the majority phase in the Na + Cs + Sb + I recipe we developed in-house does not have the same symmetry (3D confidence score of 0.05). This suggests that the target phase, the theoretically predicted double perovskite Cs_2NaSbI_6 with the Fm$\bar{3}$m space group was likely not formed under the applied experimental conditions (Table S4). Furthermore, all the synthesized Bi/Sb ternary
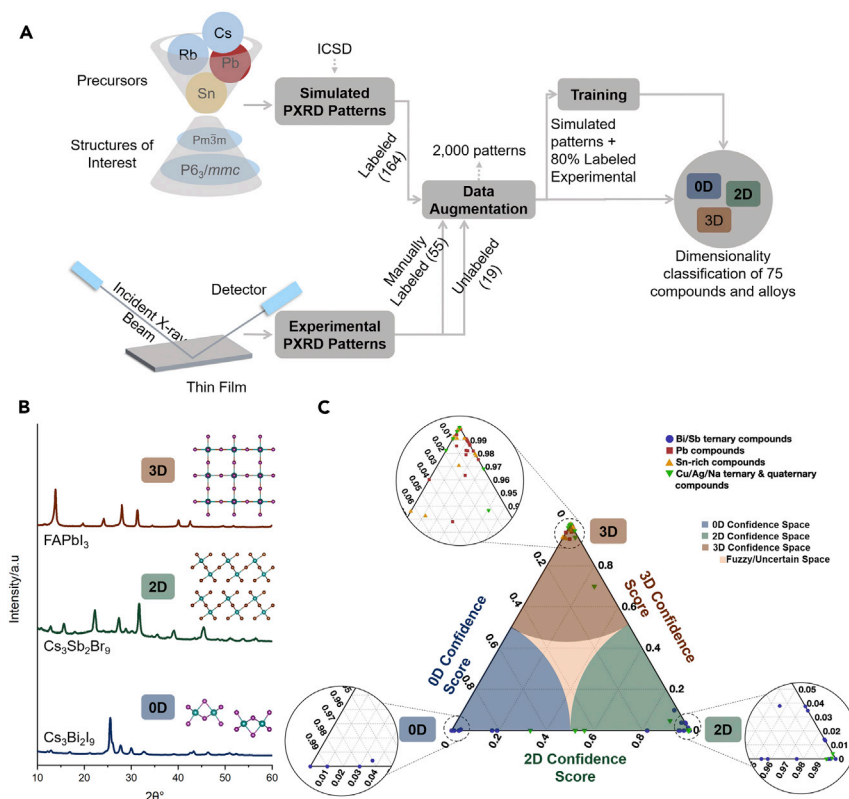
Joule

Figure 4. Machine-Learning-Assisted Analysis of the Experimentally Collected XRD Patterns

(A) A schematic workflow to employ machine-learning algorithms to assist structural characterization for perovskite-inspired materials and guide the analysis of diagnosis results. The input of the algorithm applied is the simulated and experimental PXRD patterns along with a list of precursor elements and expected crystal symmetry for target compounds. The output is the crystallographic dimensionality of the experimentally synthesized compounds.

(B) Examples of XRD patterns for 3D, 2D, and 0D perovskites. The inorganic frameworks of the molecular dimer, layered perovskite, and cubic perovskite crystal structures of interest to this study are drawn next to 0D, 2D, and 3D labels, respectively.

(C) An overview of the machine-learning-assisted structural diagnostics results. 75 unique compositions were classified into 0D, 2D, and 3D perovskites based on the crystal symmetry of the training dataset. A confidence score is associated with each output from the softmax layer in the neural network.

compounds (red) are classified to non-3D groups, which is consistent with the literature reports of $A_3B_2X_9$ (A = Cs, Rb, or MA; B = Bi or Sb; and X = I or Br). With these structural guidelines, off-line in-depth studies on the synthesis and characterization of the 19 *group 2* compositions are currently under further investigation. The machine-learning method discussed in this section provides a suggested structure type for hundreds of experimental PXRD patterns within seconds, which significantly shortens the diagnostics time, and most importantly, it enables the incorporation of structural characterization into the high-throughput cycle of learning for future laboratory design. Further discussion on algorithm performance of majority and minority classes can be found in the Supplemental Information, where we demonstrate that the approach is robust dealing with imbalanced classes. With increasing amounts of training data recorded in a future fully automated laboratory, a higher confidence score is expected to be achieved; however, samples with low confidence scores still need manual diagnostics to identify the correct structural features. Nevertheless, the introduction of machine-learning techniques to XRD diffraction analysis can be

particularly helpful for materials to undergo a phase transition, where it can be challenging to analyze multi-phase problems with manual refinement. The application of this machine-learning approach on a set of *group 2* test materials, $Cs_3(Bi_{1-x}Sb_x)_2(I_{1-x}Br_x)_9$, is shown in the next section, demonstrating a case study to extract the dimensionality for novel $A_3B_2X_9$ alloys based on PXRD patterns.

New, Tunable Materials in Thin-Film Form

With improved throughput and access to a wider range of precursors in a single growth environment, wide chemical space is explored. Here, we describe five thin-film compounds, including a previously unreported halide phase as well as four thin-film versions of 2D layered perovskites that were previously grown in bulk-crystal form. In addition, 18 inorganic lead-free perovskite alloys are characterized, more than double the reported PV thin films in this category in the literature.[3,66]

First, the signature of a double perovskite phase, $Cs_2SbAgBr_6$, was detected in the form of a thin-film mixture. We calculate a direct band gap of 1.89 eV (2.27 eV if fitting assumes indirect band gap), and the compound has been studied in depth in collaboration with Wei et al.[67] Second, upon the successful dissolution of RbBr, CsBr, $BiBr_3$, and $SbBr_3$ with annealing temperature control (Table S4), $A_3B_2Br_9$ (A = Cs or Rb and B = Bi or Sb) compounds are successfully synthesized in compact thin films via one-step solution synthesis (Figure S5). This deposition method does not require redissolving of the nanocrystals synthesized via bulk synthesis back in precursor solution to form a film, the latter has been demonstrated in previous reports.[68] 2D layered perovskite structures are confirmed for $Rb_3Bi_2Br_9$, $Rb_3Sb_2Br_9$, $Cs_3Sb_2Br_9$, and $Cs_3Bi_2Br_9$.[61] The corner-sharing double layers observed in these halide perovskites typically show a direct band gap and were reported with higher current than their 0D counterparts in PV devices.[51]

Third, we observe that the band gap is not continuous over the transition from 0D to 2D structure in the alloy series, $Cs_3(Bi_{1-x}Sb_x)_2(I_{1-x}Br_x)_9$ (x = 0.1–0.9), where the alloy has a lower band gap than either of the two end phases. The 2D Br-based $A_3B_2Br_9$ perovskites discussed in the previous paragraph are desirable for achieving higher charge transport than their 0D I-based $A_3B_2I_9$ counterparts; however, their band gap is considered to be too high for promising solar applications (>2 eV). Therefore, compositions that combine higher dimensionality and lower band gap are desirable. We herein present an important finding resulting from our materials search, demonstrating a dual-site alloy, $Cs_3(Bi_{1-x}Sb_x)_2(I_{1-x}Br_x)_9$ (x = 0.1–0.9). Figure 5A illustrates the crystal structure of the two end-members of this alloy series, $Cs_3Bi_2I_9$ and $Cs_3Sb_2Br_9$. Pawley refinement of the PXRD patterns of the thin films confirms that the two materials exhibit the 0D $P6_3/mmc$ and 2D $P-3m1$ space groups, respectively (Figure S12). The crystal structure transforms from the 0D $Cs_3Bi_2I_9$ to the 2D $Cs_3Sb_2Br_9$ with increasing $SbBr_3$ content in the precursor solution (Figure 5B). Major peak positions shift to the left due to a contraction in lattice parameters. Distinguishing between 0D and 2D $A_3B_2X_9$ compounds has been difficult based on manual phase identification from PXRD measurement since many of the peak positions overlap and only subtle differences are observed between space groups.[20,69] We are able to tell a clear 2D structure from the experimental pattern for 30% doping. Machine-learning-assisted diagnostics indicate that from around 20% Cs_3SbBr_9 dopant level, the alloy starts to show characteristics of a 2D perovskite crystallographic dimensionality.

Interestingly, while the material undergoes a structural change, there is also a non-linear dependence in the optical properties, a phenomenon that is observed for the first time in lead-free perovskite-inspired materials. The absorption edge shifts to
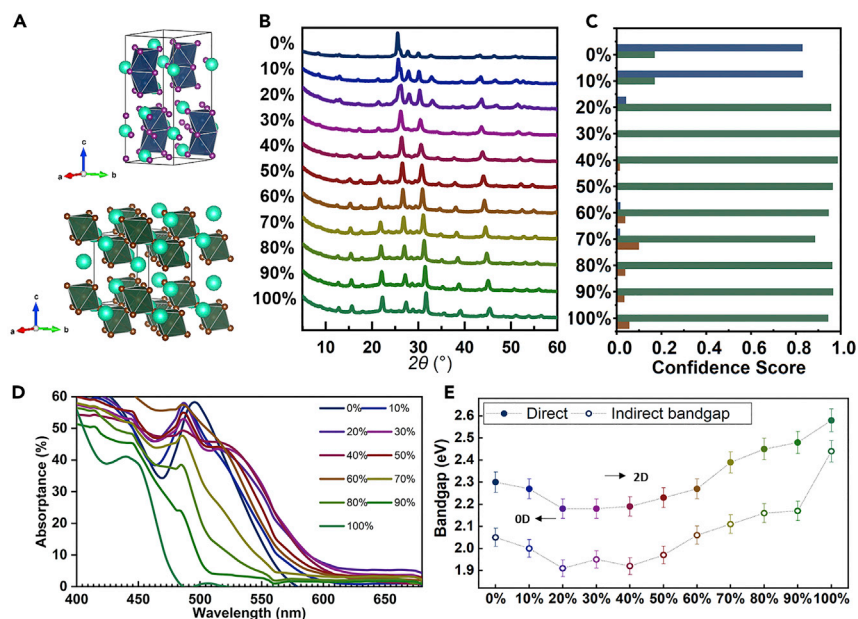
Joule

Figure 5. Crystal Structures, Structural Characterization, and Optical Properties of Cs₃(Bi₁₋ₓSbₓ)₂(I₁₋ₓBrₓ)₉

(A) Crystal structures of the 0D and 2D perovskites. Top, $Cs_3Bi_2I_9$ and bottom, $Cs_3Sb_2Br_9$.
(B and C) (B) X-ray diffraction patterns of $Cs_3(Bi_{1-x}Sb_x)_2(I_{1-x}Br_x)_9$ (x = 0–1) from the same batch and (C) indication of their crystallographic dimensionalities based on the machine-learning approach. In (C), at each doping level, the three bars represent 0D (blue), 2D (green), and 3D (brown) likelihood.
(D and E) (D) Absorptance spectra and (E) estimated band gaps of the $Cs_3(Bi_{1-x}Sb_x)_2(I_{1-x}Br_x)_9$ (x = 0–1) alloy series.

higher wavelength before switching to the other direction with more Sb and Br added (Figure 5C). A decrease in band gap is observed in the 0D region, with increasing Sb and Br content, contrary to expectations that smaller atoms result in tighter binding and larger band gaps. In the 2D alloy region, the increasing Br and Sb concentrations increase the band gap as expected, as shown in Figure 5D. With 20% $SbBr_3$ doping, the band gap was reduced to 1.9 eV assuming an indirect band gap, which is lower than that reported for $Cs_3Bi_2I_9$ and $Cs_3Sb_2I_9$.[50,51] Note that the observation of the band-gap trend is not dependent on the assumption of either direct or indirect band gap during fitting of optical absorptance data (Figure S11). Band-gap "bowing" has been observed in a number of common semiconductors, including $CdSe_xTe_{1-x}$ and $ZnSe_{1-x}Te_x$ in commercial solar cells.[70] More recently, the band-gap "bowing" behavior was observed in Pb-Sn perovskite alloys, where the non-linear band-gap trend was attributed to the mismatch in energy between atomic orbitals in Pb and Sn at the band edge.[71,72] In our Bi-Sb perovskite alloys, it is likely that a similar effect on band gap due to the alloy compositions is also present. While further investigations are underway in our laboratory, a possible mechanism for this behavior is that while the increase in the Br content in the alloys tends to increase the band gap, the chemical effects of introducing dual-site alloying reduces the overall band gap when x < 0.3.[73]

Conclusions

Here, we utilize a combination of traditional and machine-learning-aided approaches to overcome bottlenecks in materials screening and downselection, precursor development, workflow optimization, and automation of characterization

Joule

CellPress

output. We design and realize an HTE platform capable of investigating 75 unique compounds in 2 months, using 96 precursor combinations. 87% of the thin films synthesized fell within the band-gap range of 1.2 to 2.4 eV, promising for optoelectronic applications. A neural network was employed to assist in structural analysis, which achieved 90% accuracy in distinguishing the crystal dimensionality of perovskite-inspired materials in this study. This approach is fast and easy to use and assists chemists to quickly identify, for example, whether 3D perovskites were synthesized during a high-throughput screening.

With this accelerated platform, we realized four lead-free layered perovskites, $A_3B_2Br_9$ (A = Cs or Rb and B = Bi or Sb) and their multi-site inorganic alloy series $Cs_3(Bi_{1-x}Sb_x)_2(I_{1-x}Br_x)_9$ in compact thin-film form. We examine the "bowing" trend in band gaps in the alloy series and correlated this with a 0D-to-2D structural transition in crystallographic dimensionality, which was identified by machine-learning classification. Most importantly, the combination of increased experimental throughput and the successful application of statistical diagnostics provide a new paradigm to examine structure-property relationships, finding non-intuitive trends in a multi-parameter space. Such techniques have been under rapid development in recent years and will be increasingly easy to access on a daily basis for researchers in the laboratory.

EXPERIMENTAL PROCEDURES

The experimental details about the materials synthesis, UV-vis spectroscopy, and XRD characterization of thin-film samples. The neural network method and training set and the quantified workflow analysis are provided in the Supplemental Information. Experimental data of transmittance, reflectance, and XRD measurement and band-gap plots for the 75 compositions studied are available at https://github.com/acceleratedmaterials/campaign1.

SUPPLEMENTAL INFORMATION

Supplemental Information can be found online at https://doi.org/10.1016/j.joule.2019.05.014.

ACKNOWLEDGMENTS

Joule

CellPress

AUTHOR CONTRIBUTIONS

S.S., N.T.P.H., A.M.B., M.L., J.T., and J.C. performed materials synthesis. S.S., N.T.P.H., T.O., and J.T. conducted XRD measurement, D.X.C., A.M.B., and J.T. performed the optical characterization and estimated the band gaps. Z.D.R., F.O., Z.L., and S.I.P.T set up the neural network approaches to analyze XRD patterns and tested the model robustness with the assistance of S.R., B.L.D., and A.G.K. F.O. and C.S. built the training dataset with simulated XRD patterns from the ICSD database. T.B. provided the conceptual framework of the methodology and S.S., F.O., and T.B. wrote the paper. T.B., I.M.P., and J.-P.C.-B. guided the project. All authors contributed to the discussion of the results and reviewed the manuscript.

DECLARATION OF INTERESTS

The authors declare no competing interests.

REFERENCES

1. NREL, National Renewable Energy Laboratory. Best research cell efficiencies. http://www.nrel.gov/ncpv/images/efficiency_chart.jpg.

2. Abate, A. (2017). Perovskite solar cells go lead free. Joule 1, 659–664.

3. Slavney, A.H., Hu, T., Lindenberg, A.M., and Karunadasa, H.I. (2016). A bismuth-halide double perovskite with long carrier recombination lifetime for photovoltaic applications. J. Am. Chem. Soc. 138, 2138–2141.

4. Zakutayev, A., Wunder, N., Schwarting, M., Perkins, J.D., White, R., Munch, K., Tumas, W., and Phillips, C. (2018). An open experimental database for exploring inorganic materials. Sci. Data 5, 180053.

5. Stoumpos, C.C., Malliakas, C.D., and Kanatzidis, M.G. (2013). Semiconducting tin and lead iodide perovskites with organic cations: phase transitions, high mobilities, and near-infrared photoluminescent properties. Inorg. Chem. 52, 9019–9038.

6. Vargas, B., Ramos, E., Pérez-Gutiérrez, E., Alonso, J.C., and Solis-Ibarra, D. (2017). A direct bandgap copper-antimony halide perovskite. J. Am. Chem. Soc. 139, 9116–9119.

7. Zakutayev, A. (2017). Brief review of emerging photovoltaic absorbers. Curr. Opin. Green Sustain. Chem. 4, 8–15.

8. Correa-Baena, J.P., Hippalgaonkar, K., van Duren, J., Jaffer, S., Chandrasekhar, V.R., Stevanovic, V., Wadia, C., Guha, S., and Buonassisi, T. (2018). Accelerating materials development via automation, machine learning, and high-performance computing. Joule 2, 1410–1420.

9. Belsky, A., Hellenbrandt, M., Karen, V.L., and Luksch, P. (2002). New developments in the Inorganic Crystal Structure Database (ICSD): accessibility in support of materials research and design. Acta Crystallogr. B 58, 364–369.

10. Suram, S.K., Xue, Y., Bai, J., Le Bras, R., Rappazzo, B., Bernstein, R., Bjorck, J., Zhou, L., van Dover, R.B., Gomes, C.P., et al. (2017). Automated phase mapping with AgileFD and its application to light absorber discovery in the V-Mn-Nb oxide system. ACS Comb. Sci. 19, 37–46.

11. Gaultois, M.W., Oliynyk, A.O., Mar, A., Sparks, T.D., Mulholland, G.J., and Meredig, B. (2015). A recommendation engine for suggesting unexpected thermoelectric chemistries. APL Mater. 4, 053213.

12. Askerka, M., Li, Z., Lempen, M., Liu, Y., Johnston, A., Saidaminov, M.I., Zajacz, Z., and Sargent, E.H. (2019). Learning-in-templates enables accelerated discovery and synthesis of new stable double-perovskites. J. Am. Chem. Soc. 141, 3682–3690.

13. Takahashi, K., Takahashi, L., Miyazato, I., and Tanaka, Y. (2018). Searching for hidden perovskite materials for photovoltaic systems by combining data science and first principle calculations. ACS Photonics 5, 771–775.

14. Howard, J.M., Tennyson, E.M., Neves, B.R.A., and Leite, M.S. (2019). Machine learning for perovskites' reap-rest-recovery cycle. Joule 3, 325–337.

15. Jain, A., Voznyy, O., and Sargent, E.H. (2017). High-throughput screening of lead-free perovskite-like materials for optoelectronic applications. J. Phys. Chem. C 121, 7183–7187.

16. Nakajima, T., and Sawada, K. (2017). Discovery of Pb-free perovskite solar cells via high-throughput simulation on the K computer. J. Phys. Chem. Lett. 8, 4826–4831.

17. Zhao, X., Yang, D., Ren, J., Sun, Y., Xiao, Z., and Zhang, L. (2018). Rational design of halide double perovskites for optoelectronic applications. Joule 2, 1662–1673.

18. Chakraborty, S., Xie, W., Mathews, N., Sherburne, M., Ahuja, R., Asta, M., and

Mhaisalkar, S.G. (2017). Rational design: a high-throughput computational screening and experimental validation methodology for lead-free and emergent hybrid perovskites. ACS Energy Lett. 2, 837–845.

19. Zhang, P., Yang, J., and Wei, S.H. (2018). Manipulation of cation combinations and configurations of halide double perovskites for solar cell absorbers. J. Mater. Chem. A 6, 1809–1815.

20. Lee, L.C., Huq, T.N., Macmanus-Driscoll, J.L., and Hoye, R.L.Z. (2018). Research update: bismuth-based perovskite-inspired photovoltaic materials. APL Mater. 6, 084502.

21. Park, B.W., Philippe, B., Zhang, X., Rensmo, H., Boschloo, G., and Johansson, E.M.J. (2015). Bismuth based hybrid perovskites A₃Bi₂I₉ (A: methylammonium or cesium) for solar cell application. Adv. Mater. 27, 6806–6813.

22. Chen, S., Hou, Y., Chen, H., Tang, X., Langner, S., Li, N., Stubhan, T., Levchuk, I., Gu, E., Osvet, A., et al. (2018). Exploring the stability of novel wide bandgap perovskites by a robot based high throughput approach. Adv. Energy Mater. 8, 1701543.

23. Sun, S., Tominaka, S., Lee, J.-H., Xie, F., Bristowe, P.D., and Cheetham, A.K. (2016). Synthesis, crystal structure, and properties of a perovskite-related bismuth phase, (NH4)3Bi2I9. APL Mater. 4, 031101.

24. Shao, S., Liu, J., Portale, G., Fang, H.H., Blake, G.R., ten Brink, G.H., Koster, L.J.A., and Loi, M.A. (2018). Highly reproducible Sn-based hybrid perovskite solar cells with 9% efficiency. Adv. Energy Mater. 8, 1702019.

25. Gao, W., Ran, C., Xi, J., Jiao, B., Zhang, W., Wu, M., Hou, X., and Wu, Z. (2018). High-quality Cs₂AgBiBr₆ double perovskite film for lead-free inverted planar heterojunction solar cells with 2.2 % efficiency. ChemPhysChem 19, 1696–1700.

Joule

CellPress

26. Harikesh, P.C., Wu, B., Ghosh, B., John, R.A., Lie, S., Thirumal, K., Wong, L.H., Sum, T.C., Mhaisalkar, S., and Mathews, N. (2018). Doping and switchable photovoltaic effect in lead-free perovskites enabled by metal cation transmutation. Adv. Mater. 30, 29978516.

27. Filip, M.R., Liu, X., Miglio, A., Hautier, G., and Giustino, F. (2018). Phase diagrams and stability of lead-free halide double perovskites $Cs_2BB'X_6$: B = Sb and Bi, B' = Cu, Ag, and Au, and X = Cl, Br, and i. J. Phys. Chem. C 122, 158–170.

28. Curtarolo, S., Hart, G.L.W., Nardelli, M.B., Mingo, N., Sanvito, S., and Levy, O. (2013). The high-throughput highway to computational materials design. Nat. Mater. 12, 191–201.

29. Snaith, H.J. (2013). Perovskites: the emergence of a new era for low-cost, high-efficiency solar cells. J. Phys. Chem. Lett. 4, 3623–3630.

30. Granda, J.M., Donina, L., Dragone, V., Long, D.L., and Cronin, L. (2018). Controlling an organic synthesis robot with machine learning to search for new reactivity. Nature 559, 377–381.

31. Ren, F., Ward, L., Williams, T., Laws, K.J., Wolverton, C., Hattrick-Simpers, J., and Mehta, A. (2018). Accelerated discovery of metallic glasses through iteration of machine learning and high-throughput experiments. Sci. Adv. 4, eaaq1566.

32. Steinmann, V., Jaramillo, R., Hartman, K., Chakraborty, R., Brandt, R.E., Poindexter, J.R., Lee, Y.S., Sun, L., Polizzotti, A., Park, H.H., et al. (2014). 3.88% efficient tin sulfide solar cells using congruent thermal evaporation. Adv. Mater. 26, 7488–7492.

33. Brandt, R.E., Stevanović, V., Ginley, D.S., and Buonassisi, T. (2015). Identifying defect-tolerant semiconductors with high minority-carrier lifetimes: beyond hybrid lead halide perovskites. MRS Commun. 5, 265–275.

34. Jaramillo, R., Steinmann, V., Yang, C., Hartman, K., Chakraborty, R., Poindexter, J.R., Castillo, M.L., Gordon, R., and Buonassisi, T. (2015). Making record-efficiency SnS Solar cells by thermal evaporation and atomic layer deposition. J. Vis. Exp. e52705.

35. Collord, A.D., Xin, H., and Hillhouse, H.W. (2015). Combinatorial exploration of the effects of intrinsic and extrinsic defects in $Cu_2ZnSn(S,Se)_4$. IEEE J. Photovoltaics 5, 288–298.

36. Baumes, L.A., Moliner, M., and Corma, A. (2009). Design of a Full-profile-matching solution for high-throughput analysis of multiphase samples through powder X-ray diffraction. Chemistry 15, 4258–4269.

37. Park, W.B., Chung, J., Jung, J., Sohn, K., Singh, S.P., Pyo, M., Shin, N., and Sohn, K.S. (2017). Classification of crystal structure using a convolutional neural network. IUCrJ 4, 486–494.

38. Umar, F., Zhang, J., Jin, Z., Muhammad, I., Yang, X., Deng, H., Jahangeer, K., Hu, Q., Song, H., and Tang, J. (2019). Dimensionality controlling of $Cs_3Sb_2I_9$ for efficient all-inorganic planar thin film solar cells by HCl-assisted solution method. Adv. Opt. Mater. 7, 1801368.

39. Kurchin, R.C., Gorai, P., Buonassisi, T., and Stevanović, V. (2018). Structural and chemical features giving rise to defect tolerance of binary semiconductors. Chem. Mater. 30, 5583–5592.

40. Etgar, L. (2018). The merit of perovskite's dimensionality; can this replace the 3D Halide Perovskite? Energy Environ. Sci. 11 3D, 234–242.

41. Yang, T.C.J., Fiala, P., Jeangros, Q., and Ballif, C. (2018). High-bandgap perovskite materials for multijunction solar cells. Joule 2, 1421–1436.

42. Xiao, Z., Meng, W., Wang, J., Mitzi, D.B., and Yan, Y. (2017). Searching for promising new perovskite-based photovoltaic absorbers: the importance of electronic dimensionality. Mater. Horiz. 4, 206–216.

43. Quan, L.N., Yuan, M., Comin, R., Voznyy, O., Beauregard, E.M., Hoogland, S., Buin, A., Kirmani, A.R., Zhao, K., Amassian, A., et al. (2016). Ligand-stabilized reduced-dimensionality perovskites. J. Am. Chem. Soc. 138, 2649–2655.

44. Zhang, T., Long, M., Qin, M., Lu, X., Chen, S., Xie, F., Gong, L., Chen, J., Chu, M., Miao, Q., et al. (2018). Stable and efficient 3D-2D perovskite-perovskite planar heterojunction solar cell without organic hole transport layer. Joule 2, 2706–2721.

45. Saliba, M., Matsui, T., Domanski, K., Seo, J.Y., Ummadisingu, A., Zakeeruddin, S.M., Correa-Baena, J.P., Tress, W.R., Abate, A., Hagfeldt, A., et al. (2016). Incorporation of rubidium cations into perovskite solar cells improves photovoltaic performance. Science 354, 206–209.

46. Sidey, V.I., Voroshilov, Y.V., Kun, S.V., and Peresh, E.Y. (2000). Crystal growth and X-ray structure determination of $Rb_3Bi_2I_9$. J. Alloys Compd. 296, 53–58.

47. Lehner, A.J., Fabini, D.H., Evans, H.A., Hébert, C.A., Smock, S.R., Hu, J., Wang, H., Zwanziger, J.W., Chabinyc, M.L., and Seshadri, R. (2015). Crystal and electronic structures of complex bismuth iodides $A_3Bi_2I_9$ (A = K, Rb, Cs) related to perovskite: aiding the rational design of photovoltaics. Chem. Mater. 27, 7137–7148.

48. Hoye, R.L.Z., Schulz, P., Schelhas, L.T., Holder, A.M., Stone, K.H., Perkins, J.D., Vigil-Fowler, D., Siol, S., Scanlon, D.O., Zakutayev, A., et al. (2017). Perovskite-inspired photovoltaic materials: toward best practices in materials characterization and calculations. Chem. Mater. 29, 1964–1988.

49. Saidaminov, M.I., Abdelhady, A.L., Maculan, G., and Bakr, O.M. (2015). Retrograde solubility of formamidinium and methylammonium lead halide perovskites enabling rapid single crystal growth. Chem. Commun. (Camb.) 51, 17658–17661.

50. Shin, S.S., Correa Baena, J.P., Kurchin, R.C., Polizzotti, A., Yoo, J.J., Wieghold, S., Bawendi, M.G., and Buonassisi, T. (2018). Solvent-engineering method to deposit compact bismuth-based thin films: mechanism and application to photovoltaics. Chem. Mater. 30, 336–343.

51. Correa-Baena, J.P., Nienhaus, L., Kurchin, R.C., Shin, S.S., Wieghold, S., Putri Hartono, N.T., Layurova, M., Klein, N.D., Poindexter, J.R.,

Polizzotti, A., et al. (2018). A-site cation in inorganic $A_3Sb_2I_9$ perovskite influences structural dimensionality, exciton binding energy, and solar cell performance. Chem. Mater. 30, 3734–3742.

52. Lee, S., and Kang, D.W. (2017). Highly efficient and stable Sn-rich perovskite solar cells by introducing bromine. ACS Appl. Mater. Interfaces 9, 22432–22439.

53. Greul, E., Petrus, M.L., Binek, A., Docampo, P., and Bein, T. (2017). Highly stable, phase pure $Cs_2AgBiBr_6$ double perovskite thin films for optoelectronic applications. J. Mater. Chem. A 5, 19972–19981.

54. Eperon, G.E., Stranks, S.D., Menelaou, C., Johnston, M.B., Herz, L.M., and Snaith, H.J. (2014). Formamidinium lead trihalide: a broadly tunable perovskite for efficient planar heterojunction solar cells. Energy Environ. Sci. 7, 982–988.

55. Weber, D. (1978). $NH_3SnBr_xI_{3-x}$ (x=0−3), a SN(II)-system with the cubic perovskite structure. Z. Naturforsch. 33b, 862–865.

56. Jeon, N.J., Noh, J.H., Kim, Y.C., Yang, W.S., Ryu, S., and Seok, S.I. (2014). Solvent engineering for high-performance inorganic–organic hybrid perovskite solar cells. Nat. Mater. 13, 897–903.

57. Boix, P.P., Soci, C., Mathews, N., Yin, J., Grätzel, M., Baikie, T., et al. (2016). $MA_2CuCl_xBr_{4-x}$ hybrid perovskites. Inorg. Chem. 55, 1044–1052.

58. Tauc, J. (1968). Optical properties and electronic structure of amorphous Ge and Si. Mater. Res. Bull. 3, 37–46.

59. Slimi, B., Mollar, M., Ben Assaker, I., Kriaa, A., Chtourou, R., and Marí, B. (2017). Synthesis and Characterization of perovskite $FAPbBr_3−xIx$ thin films for solar cells. Monatsh. Chem. 148, 835–844.

60. Chabot, B., and Parthe, E. (1978). $Cs_3Sb_2I_9$ and $Cs_3Bi_2I_9$ with the hexagonal $Cs_3Cr_2Cl_9$ structure type. Acta Crystallogr. 34, 645–648.

61. Peresh, E.Y., Sidei, V.I., Zubaka, O.V., and Stercho, I.P. (2011). K2 (Rb2,Cs2,Tl2)TeBr6(I6) and Rb3(Cs3)Sb2(Bi2)Br9(I9) perovskite compounds. Inorg. Mater. 47, 208–212.

62. Oviedo, F., Ren, Z., Sun, S., Settens, C., Liu, Z., Hartono, N.T.P., Savitha, R., DeCost, B.L., Tian, S.I.P., Romano, G., et al. (2019). Fast classification of small X-ray diffraction datasets using data augmentation and deep neural networks. Comp. Mater. 5, 60.

63. Pedregosa, F., Varoquaux, G., Gramfort, A., Michel, V., Thirion, B., Grisel, O., Blondel, M., Prettenhofer, P., Weiss, R., Dubourg, V., et al. (2011). Scikit-learn: machine learning in Python. J. Mach. Learn. Res. 12, 2825–2830.

64. LeCun, Y., Bengio, Y., and Hinton, G. (2015). Deep learning. Nature 521, 436–444.

65. Bottou, L., and Bousquet, O. (2008). The tradeoffs of large scale learning. Adv. Neural Inf. Process. Syst. 20, 161–168.

66. Gupta, S., Bendikov, T., Hodes, G., and Cahen, D. (2016). A lead-free halide perovskite for

Joule

CellPress

long-term solar cell application. Insights on SnF2Addition. ACS Energy Lett. *1*, 1028–1033.

67. Wei, F., Deng, Z., Sun, S., Hartono, N.T.P., Seng, H.L., Buonassisi, T., Bristowe, P.D., and Cheetham, A.K. (2019). Enhanced visible light absorption for lead-free double perovskite $Cs_2AgSbBr_6$. Chem. Commun. (Camb.) *55*, 3721–3724.

68. Leng, M., Yang, Y., Zeng, K., Chen, Z., Tan, Z., Li, S., Li, J., Xu, B., Li, D., Hautzinger, M.P., et al. (2018). All-inorganic bismuth-based perovskite quantum dots with bright blue photoluminescence and excellent stability. Adv. Funct. Mater. *28*, 1704446.

69. Chang, J.H., Doert, T., and Ruck, M. (2016). Structural variety of defect perovskite variants $M_3E_2X_9(M = Rb, Tl, E = Bi, Sb, X = Br, I)$. Z. Anorg. Allg. Chem. *642*, 736–748.

70. Tit, N., Obaidat, I.M., and Alawadhi, H. (2009). Origins of bandgap bowing in compound-semiconductor common-cation ternary alloys. J. Phys. Condens. Matter *21*, 075802.

71. Goyal, A., McKechnie, S., Pashov, D., Tumas, W., van Schilfgaarde, M., and Stevanović, V. (2018). Origin of pronounced nonlinear band gap behavior in lead-tin hybrid perovskite alloys. Chem. Mater. *30*, 3920–3928.

72. Abdelhady, A.L., Saidaminov, M.I., Murali, B., Adinolfi, V., Voznyy, O., Katsiev, K., Alarousu, E., Comin, R., Dursun, I., Sinatra, L., et al. (2016). Heterovalent dopant incorporation for bandgap and type engineering of perovskite crystals. J. Phys. Chem. Lett. *7*, 295–301.

73. McCall, K.M., Stoumpos, C.C., Kontsevoi, O.Y., Alexander, G.C.B., Wessels, B.W., and Kanatzidis, M.G. (2019). From 0D Cs3Bi2I9 to 2D Cs3 Bi2I6Cl3: dimensional expansion induces direct bandgap but enhances electron-phonon coupling. Chem. Mater. acs.chemmater.9b00636.